Raman scattering measurements of molecular hydrogen in a low-density, arc-heated plasma

D.R. Beattie, M.A. Cappelli[*]

High Temperature Gasdynamics Laboratory, Stanford University, Stanford, CA 94305-3032, USA
(Fax: +1-650/723-1748, E-mail: cap@leland.stanford.edu)

Abstract. Raman scattering measurements of molecular hydrogen density and temperature were made in a low-density, arc-heated plasma flow. Pulsed-laser excitation was used to improve the signal-to-noise ratio in this high-background environment. Quantum-limited detection was achieved through the use of gated photon counting and a high-power Nd:YAG laser. Radial profiles of rotational temperature and density at the exit plane were measured for five power levels. In all cases the profiles were asymmetric about the centerline. The rotational temperatures were compared with the translational temperatures of atomic hydrogen from LIF studies and found to be slightly lower. This result suggests that this flow, like the cold flow, is not in translational–rotational equilibrium.

PACS: 52.25.-b; 52.70.-m; 52.30.-9

Arcjets use a direct current dc arc to heat an incoming gas stream which is expanded through a supersonic nozzle. These devices have a number of applications including spacecraft propulsion and materials synthesis. As space propulsion devices, arcjet thrusters offer higher exhaust velocities thanconventional chemical rockets and are now being employed in station-keeping roles on communication satellites. There is a desire to increase both the thermal efficiency and exhaust velocities of current designs and to develop higher thrust versions which could be used in applications such as orbit transfer. Such improvements will depend partly on a better understanding of the plasma and gas dynamic processes undergone in the arcjet nozzle.

Currently both numerical analysis and experimental studies are being used to investigate flow properties in low-power arcjet thrusters. Attempts at modeling the plasma flow in pure hydrogen arcjet thrusters use both continuum [1–3] and Monte Carlo techniques [4]. These models are useful in understanding the various loss mechanisms in an arcjet, including anode radiation, ionization, dissociation, and other frozen-flow losses. However, experimental measurements of relevant physical parameters in both the nozzle and plume

are needed to validate these models. Of particular interest are density, temperature, and velocity measurements of atomic hydrogen (H) and molecular hydrogen (H_2).

Recent studies have relied primarily on optical diagnostics such as emission, absorption, and fluorescence. Optical techniques have the potential advantages of high spatial resolution and minimal perturbation to the flow field and most efforts have probed atomic hydrogen because of the large number of transitions in the visible spectrum. These experiments have included measurements of: H velocity and translational temperature using laser-induced fluorescence (LIF) of the H_α Balmer line [5, 6], H density using vacuum ultraviolet absorption [7], and multi-photon LIF [8, 9], and H temperature and electron density using emission [10].

Molecular hydrogen (like other homonuclear, diatomic molecules) does not undergo radiative transitions between rotational or vibrational levels in the ground electronic state since it does not have a dipole moment. As a result, one can not use emission, absorption, or fluorescence techniques to study these energy states. Until now, measurements of H_2 properties have been limited to spatially averaged absorption measurements [11] and density and temperature measurements in the distant plume using mass sampling spectroscopy [12]. However, numerical simulations (Butler et al. 1994) have predicted that ≈ 95% of the mass flow at the exit plane is molecular hydrogen so it is important to have experimental data on H_2 exit-plane properties.

The research described in this paper involved making measurements of molecular hydrogen properties in the plume of a hydrogen arcjet thruster. Spontaneous Raman scattering was chosen as a suitable technique for making spatially resolved temperature and density measurements of the ground electronic state of H_2. The primary disadvantage of Raman scattering is that the low signal levels are difficult to detect in a luminous background.

In this study, the population of various rotational levels was measured, giving the rotational temperature and density. Initial measurements [13] in the plume of a cold-flowing arcjet thruster were compared with the results of Monte Carlo numerical simulations [3] and showed significant translational–rotational nonequilibrium.

---

[*]Corresponding author.

1 Theory

1.1 Raman scattering

The Raman effect is a linear, inelastic, two-photon scattering process. An incident photon of frequency v_0 scatters off a particle, causing a transition in the particle from the initial state i to a final state f. Since the system energy is conserved, the scattered photon must be shifted in energy correspondingly:

$$\varepsilon_{mol,i} + \varepsilon_{v,i} = \varepsilon_{mol,f} + \varepsilon_{v,f}$$
$$\Delta\varepsilon_v = -\Delta\varepsilon_{mol}, \tag{1}$$

where ε_{mol} and ε_v are the energy of the molecule and photon, respectively. In the harmonic oscillator/rigid rotor approximation, the molecular energy can be written as:

$$\varepsilon_{mol} = \varepsilon_{trans} + \varepsilon_{rot} + \varepsilon_{vib} + \varepsilon_{elec} + \varepsilon_{nucl}. \tag{2}$$

The Raman transitions under consideration here all begin and end in the ground electronic state. Furthermore, changes in the translational and nuclear energy components as a result of the Raman scattering process are small. Hence the changes in ε_{mol} can be approximated as changes in the rotational and vibrational states, allowing (1) to be written as:

$$\Delta\varepsilon_v = -\Delta\varepsilon_{mol}(v, J), \tag{3}$$

For a diatomic molecule, the selection rules are $\Delta J = 0, \pm 2$ and $\Delta v = 0, \pm 1$, where $\Delta J = J_f - J_i$ and $\Delta v = v_f - J_i$. The case of $\Delta J = 0$ and $\Delta v = 0$ is actually Rayleigh scattering. Scattering is designated as purely rotational when $\Delta J = \pm 2$ and $\Delta v = 0$, purely vibrational when $\Delta J = 0$ and $\Delta v = \pm 1$, and rotational–vibrational when $\Delta J = \pm 2$ and $\Delta v = \pm 1$.

Theoretical Raman spectra were calculated for H_2 in equilibrium at a given temperature and density. The Raman energy shifts were taken from the experimentally-measured values of Veirs and Rosenblatt [14] for pure rotational, vibrational and rotational–vibrational transitions from $v_i = 0$ and $J_i = 0$ through $J_i = 5$ (6 for Q branch). These measurements are in excellent agreement with the quantum mechanical calculations of Wolniewicz [15], differing by less than one part in 10^5.

The H_2 Raman line shape is primarily determined by Doppler and collisional effects [16]. At the low pressures in these experiments (typically 40–50 Pa), the transitions will be primarily Doppler-broadened. The Doppler width for Raman scattering is different than for emission or absorption, since two photons are involved. By solving the equations of conservation of energy and momentum, Weber [17] shows that the Doppler width is:

$$\Delta v_{FWHM} = \frac{2}{c}\left(2\ln\frac{2kT}{m_{mol}}\right)^{\frac{1}{2}}\left[4(v_0^2 + v_0\Delta v_R)\sin^2\frac{\theta}{2} + \Delta v_R^2\right]^{\frac{1}{2}}, \tag{4}$$

where θ is the angle between the incident and scattered light ($\theta = 180°$ implies forward scattering), Δv_R is the Raman frequency shift, and FWHM denotes the full-width at half maximum.

Raman cross sections for transitions from $v_i = 0$ and $J_i = 0$ through $J_i = 3$ were calculated by Ford and Browne [18] using quantum mechanical evaluations of the dynamic polarizability. Their results are in good agreement with previous experimental measurements and calculations. The cross sections were obtained at the excitation wavelength of interest using their 8th-order expansion in wavelength. Cross sections for states $J_i = 4$ and higher were not available, so they were estimated from the $J_i = 3$ value taking into account the v_R^3 frequency dependence.

1.2 Scattering predictions for molecular hydrogen

In a typical Raman experiment, the incident photons are provided by a laser beam at a rate $\dot{N}_L$, and light scattered into a solid angle $d\Omega$ is collected from a beam segment of length l. The rate of Raman photons scattered for a transition from the initial state i to the final state f is:

$$\dot{N}_{i,f} = \dot{N}_L l n_0 \frac{n_i}{n_0}\left(\frac{d\sigma}{d\Omega}\right)_{i,f} d\Omega, \tag{5}$$

where n_0 is the molecular number density, n_i/n_0 is the population fraction in the initial state, and $(d\sigma/d\Omega)_{i,f}$ is the differential Raman cross section for the transition from i to f.

The population fractions n_i/n_0 were calculated assuming the gas was in local thermodynamic equilibrium (LTE) with the molecules obeying Boltzmann statistics, in which case:

$$\frac{n_i}{n_0} = \frac{g_i\,e^{-\varepsilon_i/kT}}{\sum_i g_i\,e^{-\varepsilon_i/kT}} = \frac{g_i\,e^{-\varepsilon_i/kT}}{q}, \tag{6}$$

where q is the molecular partition function. Neglecting interactions between all energy modes except rotational and nuclear, the total molecular wavefunction for H_2 may be expressed as follows:

$$\Psi_{total} = \Psi_{trans}\Psi_{vib}\Psi_{elec}\Psi_{rot,\,nucl}, \tag{7}$$

which implies:

$$\varepsilon_{total} = \varepsilon_{trans} + \varepsilon_{vib} + \varepsilon_{elec} + \varepsilon_{rot,\,nucl}. \tag{8}$$

Hence the partition function can be factored as follows:

$$q = q_{trans} + q_{elec} + q_{vib} + q_{rot,\,nucl}. \tag{9}$$

allowing the population fraction for a particular state of an energy mode to be calculated independently of the other modes. For example, the population fraction in the vibrational state v is:

$$\frac{n(v)}{n_0} = \frac{g_{vib}(v)\,e^{-\varepsilon_{vib}(v)/kT}}{\sum_v g_{vib}(v)\,e^{-\varepsilon_{vib}(v)/kT}}, \tag{10}$$

which only requires knowledge of the vibrational energy levels and degeneracies. The vibrational populations were calculated using the harmonic-oscillator approximation with $\Delta\varepsilon_{vib}(v = 0 \rightarrow v = 1)$ from Wolniewicz [15] used as the vibrational energy constant. The error introduced by making the harmonic approximation is small at the temperatures involved

in this study, since most of the molecules are in the ground vibrational state ($> 95\%$ at $T < 2000$ K). The rotational energies were taken from a 6-parameter fit to experimental data provided by Jennings et al. [19]. These energy levels agree to better than 1 part in 10^4 with the previously mentioned results of Veirs and Rosenblatt [14] and Wolniewicz [15]. The electronic partition function was taken as unity. Furthermore, all measurements taken were integrated over essentially all translational velocities, so the translational partition function can be neglected.

Unlike the other energy modes, the rotational and nuclear modes interact, so their populations may not be calculated independently. A hydrogen nucleus (proton) is a fermion with spin of $I = 1/2$. As a result, the wavefunction of a H_2 molecule must be antisymmetric with respect to interchange of the two nuclei. This property results in a restriction on the symmetry of the rotational wavefunction. For H_2 in the ground electronic state, the electronic wavefunction is symmetric. In addition, the translational and vibrational wavefunctions are both symmetric. The only components of Ψ_{total} which can be antisymmetric are Ψ_{nucl} and Ψ_{rot}. There are four possible nuclear spin states of the two nuclei: three symmetric states with parallel spins (often referred to as ortho-hydrogen), and one antisymmetric state with opposed spins (para-hydrogen). The rotational wavefunctions are symmetric for even J and antisymmetric for odd J. Hence there are only two ways of satisfying the antisymmetric constraint on the total wavefunction: (i) coupling a symmetric nuclear spin state (ortho) with an antisymmetric rotational state (odd J) or (ii) coupling the antisymmetric nuclear spin state (para) with a symmetric rotational state (even J).

The rotational-nuclear partition function is calculated as follows:

$$q_{rot, nucl} = \sum_{J=0}^{\infty} g_{nucl} g_{rot} e^{-\varepsilon_{rot}/kT} , \qquad (11)$$

where g_{rot} is the rotational degeneracy $(2J + 1)$, g_{nucl} is the nuclear degeneracy (3 for odd J, 1 for even J), and the nuclear state energy ε_{nucl} is neglected. The nuclear degeneracy ratio of 3:1 (ortho-para) results in a 3:1 statistical weighting of the odd-even J states. At temperatures above 300 K, the upper rotational states are sufficiently populated in equilibrium that the ortho-para ratio is in fact 3:1. At lower temperatures, the population increasingly fills the $J = 0$ state, and the equilibrium ortho-para ratio decreases. In the limit as T approaches 0, the equilibrium ortho-para ratio also approaches 0.

Using the previously outlined techniques, the predicted signal from H_2 at reference conditions ($T = 300$ K, $P = 101\,325$ Pa) is shown in Fig. 1 for various rotational and/or vibrational transitions from $v_i = 0$. The plot shows the intensity versus wavelength for excitation by a 2-W laser at 532 nm, with $l = 2$ mm, $d\Omega = 0.024$ sr, and a detection system efficiency (detected photons per collected photon) of $\eta_{sys} = 0.005$. The Rayleigh line is shown for comparison, though it is ≈ 1000 times more intense than the strongest Raman transition. The lowest four rotational states are shown, since they are the only ones with a significant population at this temperature. The pure rotational transitions, near the Rayleigh line, are the most intense at up to 6000 photon s^{-1}. However the slightly weaker pure vibrational transitions near
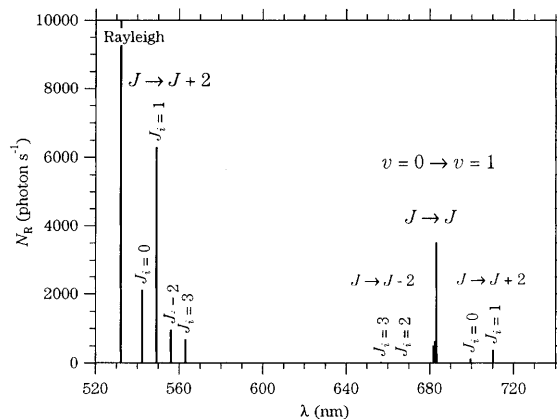

Fig. 1. Predicted Raman intensity versus wavelength for various rotational and/or vibrational transitions from H_2 at reference conditions (pure molecular hydrogen, $T = 300$ K, $P = 101\,325$ Pa)

680 nm were used in these experiments for two reasons. First, they are well separated from the laser wavelength, which makes it easier to separate them from elastically scattered light due to both Rayleigh scattering and reflections off the arcjet and chamber walls. Second, since the various transitions are close together they can be measured in a single, short spectral scan. These transitions are shown in more detail in the top frame of Fig. 2. To indicate how these features might appear with typical instrument resolution, the spec-
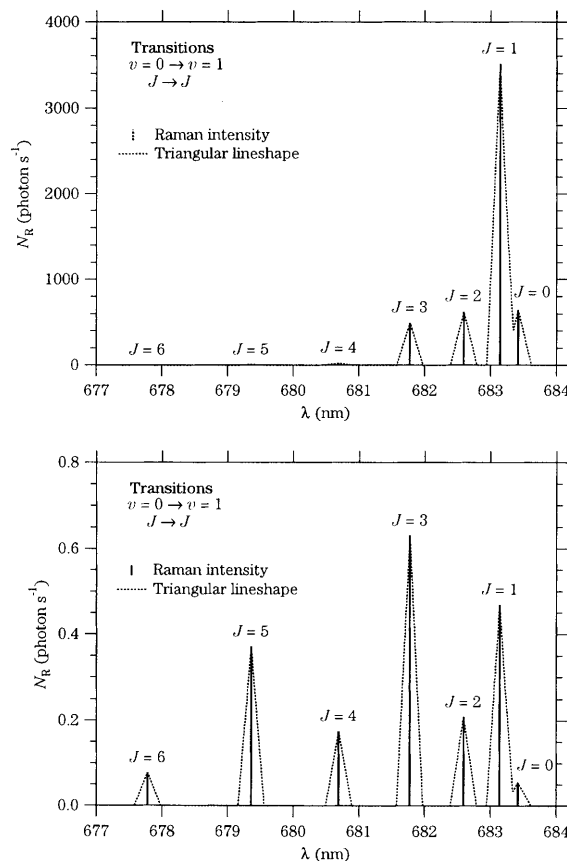

Fig. 2. Predicted Raman intensity versus wavelength for pure vibrational transitions. *Top*: under the same conditions as Fig. 1. *Bottom*: at conditions typical at the arcjet exit under nominal arc-ignited operation

Table 1. Summary of Raman transition data at reference conditions using an incident wavelength of 532.1 nm, with the Q-branch transitions highlighted

| v_i	v_f	J_i	J_f	λ/ nm	$\Delta\varepsilon_R/hc$/ m^{-1}	n_i/n_0	σ/ 10^{-33} m^2	$\dot{N}_R$/ s^{-1}
0	0	0	2	542.326	35 437	0.128	3.292	2115.4
0	0	1	3	549.258	58 709	0.657	1.914	6295.7
0	0	2	4	556.204	81 446	0.117	1.635	960.3
0	0	3	5	563.102	103 470	0.092	1.485	682.5
0	1	0	0	683.421	416 120	0.128	1.000	642.5
0	1	1	1	683.145	415 528	0.657	1.067	3509.1
0	1	2	2	682.595	414 349	0.117	1.065	625.7
0	1	3	3	681.777	412 590	0.092	1.079	495.8
0	1	4	4	680.695	410 259	0.004	1.084	23.1
0	1	5	5	679.359	407 370	0.001	1.090	5.5
0	1	6	6	677.782	403 945	0.000	1.098	0.1
0	1	0	2	699.515	449 785	0.128	0.201	128.9
0	1	1	3	710.201	471 294	0.657	0.117	383.6
0	1	2	4	720.646	491 703	0.117	0.032	18.5
0	1	3	5	730.725	510 842	0.092	0.021	9.9
0	1	2	0	667.263	380 686	0.117	0.023	13.6
0	1	3	1	656.805	356 824	0.092	0.032	14.6
0	0	0	0	532.100	0	0.128	109.403	70310.4
0	0	1	1	532.100	0	0.657	111.182	365710.2
0	0	2	2	532.100	0	0.117	111.462	65460.9
0	0	3	3	532.100	0	0.092	112.522	51714.8

trum was also convolved with a triangular function of 0.2 nm FWHM. Under these conditions, all the peaks are resolved except $J = 0$ and $J = 1$. However, only the wings of these two lines overlap and the centerline intensity is unaffected by the adjacent transition. Table 1 shows a summary of these calculations, including the transition wavelengths, cross sections, and intensities. Rayleigh scattering information is included for comparison.

In order to determine if Raman scattering is a feasible technique for use in the arcjet plume, Raman spectra were calculated for the estimated flow conditions. The average exit-plane density was estimated at 1×10^{22} m^{-3} using 6000 m s^{-1} as a typical mass-averaged exhaust velocity. The rotational temperature was estimated to be 1500 K based on the absorption measurements of Pollard [12]. Using these conditions, the spectrum shown in the bottom frame of Fig. 2 was calculated using the same setup parameters as for the reference calculation. The maximum estimated signal level is 0.6 photon s^{-1} from the $J = 3$ transition. At these higher temperatures, the population is spread out over more rotational levels, with significant population in all seven of the rotational states shown. The coupling of the rotational degeneracy to the nuclear spin degeneracy is evident from the alternating high-low intensity of the odd–even transitions. These very low signal estimates suggest that detection of the Raman scattering will be difficult, especially in the highly luminous background of the plume. Long collection periods will likely be required in order to accumulate statistically significant data.

2 Experiment

2.1 Arcjet

The arcjet thruster uses an electric arc to heat propellant to high temperatures, often 10 000 to 20 000 K. The hot gases
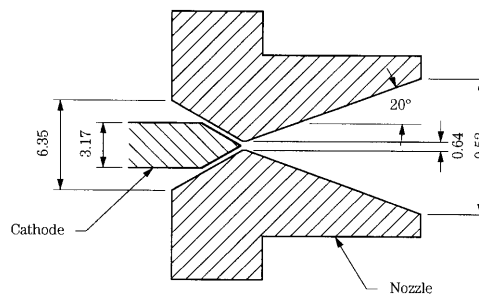
Fig. 3. The 1-kW-class arcjet nozzle and cathode, showing key dimensions in mm

are then expanded through a Laval nozzle. The arc passes from the cathode to the nozzle walls, which act as the anode. The arcjet nozzle is machined from a tungsten alloy containing 98% W and 2% Th. Both the converging and diverging sections are conical, with half angles of 30° and 20° respectively. The nozzle diverging section has a 225:1 area ratio relative to the 0.64-mm − diameter throat. The cathode is machined from a rod of the same alloy, with a tip angle matching that of the converging section. The cathode is installed by placing it in contact with the converging section, then pulling it 0.7 mm back. The nozzle is shown in Fig. 3. The anode is held by a stainless-steel anode housing which is bolted to the anode body. The cathode is insulated from the housing with a boron nitride sleeve. The hydrogen is injected tangentially through two small passages in the injector disk upstream of the cathode tip. The swirl imparted by this injection mechanism is believed to help stabilize the arc, primarily during startup.

The arcjet thruster was operated in a vacuum chamber 1.09 m long and 0.53 m in diameter with optical access through 75-mm-diameter ports. It was mounted on a two-axis axial and radial translation stage. Twelve optical ports were located at 30° intervals around the circumference of the tank, with additional ports in the endwall. The tank was evacuated by two Roots blowers backed by mechanical roughing pumps with a total capacity of 1.2 m^3 s^{-1}. This system was capable of maintaining a back pressure of 43 ± 2 Pa while flowing 13.3 mg s^{-1} hydrogen.

2.2 Optical setup

In the previous cold-flow experiments [3, 13, 20], a cw laser was used as an excitation source. However, in order to improve the signal-to-noise ratio (SNR), a pulsed laser excitation scheme was chosen here. The Nd:YAG laser used was a Spectra Physics DCR-1 flashlamp-pumped, solid-state model. The output was frequency doubled using a type-II KDP crystal, and the 532-nm light was separated using two dichroic niters. When operating at a 10-Hz repetition rate, the laser was capable of producing 200-mJ pulses at 532 nm with a 10-ns length.

Initially, the laser beam was sent axially into the arcjet through a port in the chamber endwall, as in the cold-flow experiments. However, the beam intensity at nozzle was so high that each laser pulse created a tungsten plasma and after a relatively short period of time, the nozzle was visibly eroded by the laser. In order to allow full laser energy to be utilized,
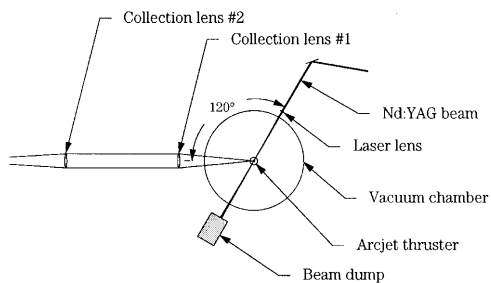
Fig. 4. Schematic diagram of laser and collection optics (front view)

the setup was modified to send the laser beam radially into the arcjet plume. The laser was sent in through a port 30° from vertical and directly out through the opposite port (Fig. 4).

The scattered light was collected at $\theta = 120°$ through a port located in the same circumferential plane as the laser at optical table level, and was focused onto a spectrometer entrance slit with an achromatic two-lens system as shown Fig. 5. The collection lens ($f = +400$ mm, $d = 76$ mm) was limited to $f/5.7$ by the port geometry. The focusing lens ($f = +600$ mm, $d = 76$ mm) was chosen to match the spectrometer f-number. The spatial resolution was 2 mm in the radial direction, determined by the slit height, and 0.25 mm in the axial direction, determined by the slit width. The spectrometer was a 1.0-m-focal-length $f/8.7$ single-pass Czerny–Turner design (Jarrell Ash 78-466).The grating was an 1800-line/mm holographic model with high efficiency from 400 to 1000 nm. A long-pass filter (Schott OG 590) was placed before the entrance slit to further reduce the intensity of collected laser light to negligible levels. The spectrometer slits were 400 μm giving a spectral resolution of ≈ 0.2 nm.

Light was detected at the exit slits with a Hamamatsu R928 photomultiplier tube (PMT) which had an efficiency of 6% at 680 nm and was operated at 1000 V. The output was amplified by an integral socket/preamplifier assembly (Hamamatsu C716-01) and sent to a photon counter (SRS 400). The counter was triggered by the laser using a photodiode. The 15-ns gate width was as narrow as possible to maximize the background rejection while still being wide enough to capture the peak of the signal pulse including jitter. The gate delay was first set approximately by simultaneously monitoring the counter input signal and the gate output on a two-channel oscilloscope. To set it more accurately, the count rate was recorded for a constant level of pulsed-light input to the detector. The delay was then scanned over the
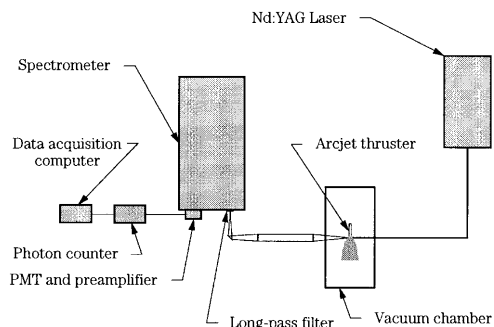
time-frame of interest and set at the position of the maximum count rate. The counter was gated to the laser pulse using a photodiode. Counts are only accumulated when the counter is gated. The photon pulse height distribution peaked at ≈ 300 mV and the lower level discriminator was set to 100 mV. The spectrometer was scanned over the spectral region of interest and the photon counter output was recorded on a 486 computer using SRS 440 software.

The system was calibrated for absolute efficiency by measuring the Raman scattering from stagnant H_2 at a known temperature and pressure. In order to account for the different efficiency at each transition, the relative efficiency versus wavelength was measured using a tungsten strip lamp. This second calibration was necessary since the transitions from $J = 4$ through 6 were too weak at room temperature to be accurately measured.

3 Results and analysis

Given the low signal levels expected in the arc-ignited flow, it was feasible to make measurements at only a few spatial positions. Since arcjet performance is determined entirely by the exit-plane properties, data were collected as close to the exit as possible. Measurements were taken at five radial locations each 2 mm apart. With spatial resolution of 2 mm radially, this mesh covered the entire exit plane with no overlapping of segments. The arcjet was positioned at $z = +4.0$ mm and the data acquisition program was started. The signal was recorded for 4000 laser pulses (≈ 400 s) at each of the five positions across the exit plane.

Radial profiles in the arcjet plume were taken at five power levels: 800, 900, 1000, 1200, and 1400 W. With the hydrogen mass flow at 13.3 mg s^{-1} , the corresponding specific power levels were from 60 MJ kg^{-1} to 106 MJ kg^{-1}. A plot of the Raman signal versus radial position for the 900 W case is shown in Fig. 6. The signal levels ranged from under 300 photons (0.7 photons^{-1}) from state $J = 1$ to 5 photons (0.01 photons^{-1}) from $J = 6$. One notable feature is that the data is not symmetrical about $z = 0$. This asymmetry was observed at all power levels, although to varying degrees. In order to determine if this effect was systematic, one data set was taken by scanning the arcjet up for some J values and down for the others. However, there was no correlation be-

Fig. 5. Schematic diagram of experimental apparatus (plan view)
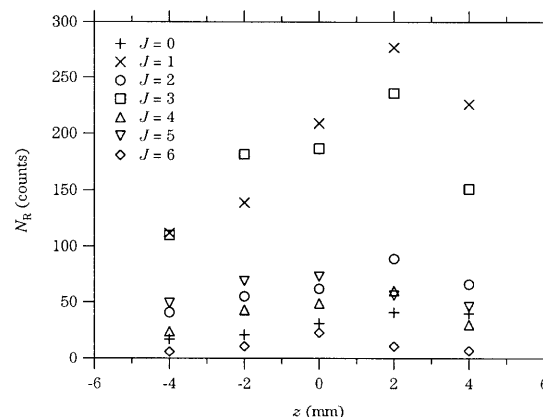

Fig. 6. Experimental Raman signal versus radial position at 900 W power

tween the scan direction and the asymmetry. Furthermore, the plume emission provided confirmation that the arcjet was properly centered. The plume emission that was measured simultaneously with the Raman scattering using the cw gate is shown in Fig. 7 for the 900 W case. Gaussian curves were fitted to the emission to check the centering and in all cases the center of the fit was within 50 μm of $z = 0$. The emission intensity varied with J depending on whether the Raman transition wavelength coincided with any H_2 emission lines.

The first step in the analysis was to correct the data for possible saturation effects, which arise when consecutive photons overlap within the temporal resolution of the photon counting electronics [19]. This correction was negligible except in the calibration scans, where the $J = 1$ peak was reduced $\approx 20\%$ by saturation. Next, the contribution of the cw signal to the gated counts was subtracted, using the measured cw rejection ratio of 6.4×10^6. This amount was no more than 4 counts at the 1400 W power level and less than 1 count at 800 W. With signal levels typically 40 to 200 counts, the largest source of error was the statistical variation in N_R, with the SNR equal to $\sqrt{N_R}$. The raw data was normalized by the laser power and relative efficiency at each transition. Then a best fit was performed to the corrected data using a function which assumed that the flow was in local thermodynamic equilibrium (LTE) with rotational population distributions dictated by a rotational temperature. The two parameters in this fit (LTE fit) were the H_2 temperature and density. For the data presented here, states $J = 0$ through 3 were used for calibration and states $J = 0$ through 6 were used in the plume.

The corrected calibration data and LTE fit intensities are plotted as a function of wavelength in Fig. 8 and in a Boltzmann plot in Fig. 9. The data in Fig. 8 is normalized by the laser pulse energy in Joules (J). The excellent agreement is primarily due to the good SNR afforded by the relatively high density at 100 Pa. The LTE fit temperature of 303 ± 9 K is consistent with the measured room temperature of 300 K. The intensity of the transitions from $J = 4$ through $J = 6$ are shown for the LTE fit, but were not measured because of their relative weakness at this temperature.

Figure 10 shows a plot of the corrected data from Fig. 6 at $z = 0$ mm along with the results of the LTE fit. As an indi-

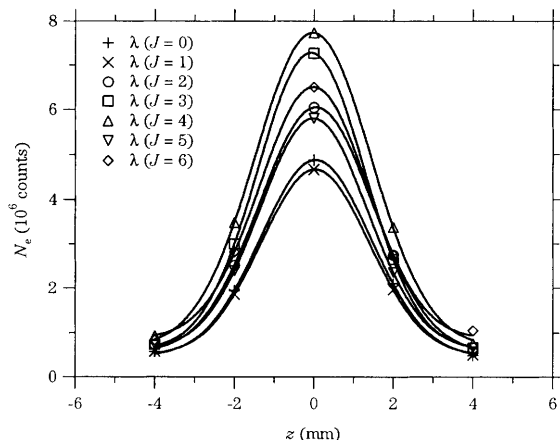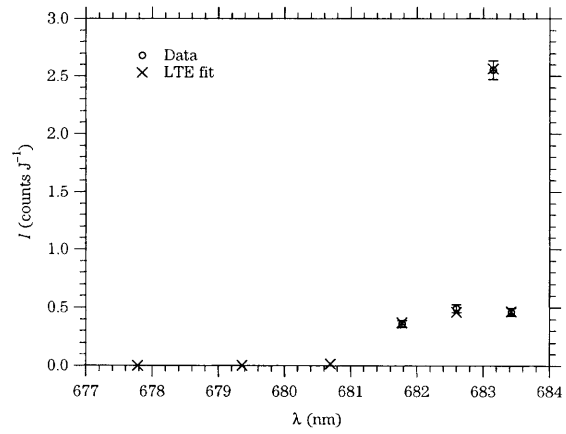**Fig. 8.** Normalized experimental Raman signal versus wavelength from calibration data
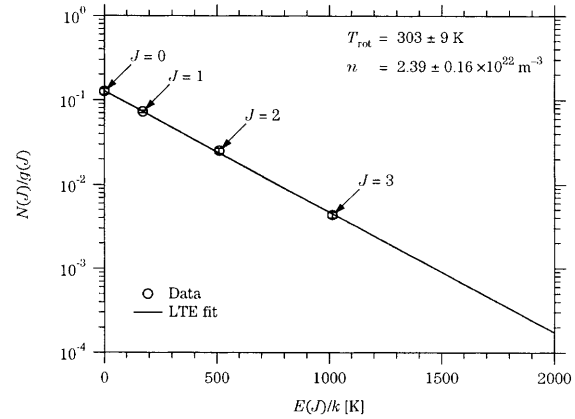

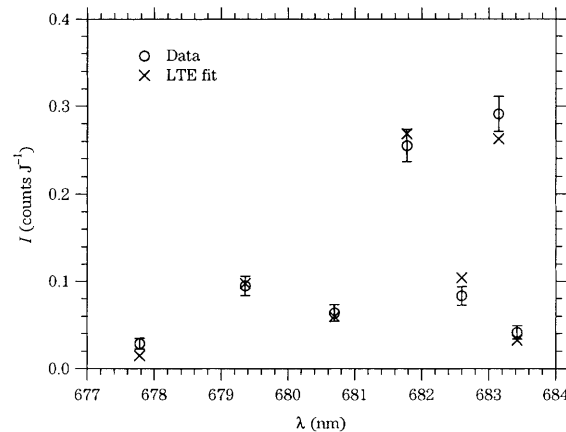**Fig. 9.** Boltzmann plot of measured rotational population fractions from Fig. 8

Fig. 10. Normalized Raman signal versus wavelength measured at $x = 2$ mm and $z = 0$ mm while operating at $P = 900$ W

cation of how weak the scattering process is, the normalized peak signal of 0.3 photon J^{-1} corresponds to 1 detected photon for every 10^{19} laser photons. The corresponding Boltzmann plot of the data is shown in Fig. 11. This data was typical in that all but two or three points fell within one standard error of the intensity fit. For data following a Poisson distribution, one would expect measurements to lie within
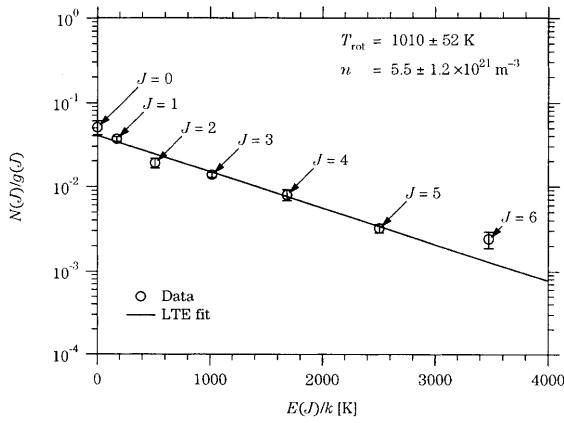

Fig. 7. Plume emission signal measured simultaneously with the Raman signal shown in Fig. 6

Fig. 11. Boltzmann plot of experimental data in Fig. 11, showing the measured density and rotational temperature, along with the calculated pressure

Fig. 13. Measured H_2 density versus radial position for the 900-W power level

one standard error 68% of the time (for large N). Thus the observed agreement of the data with the fit is quite reasonable.

The temperature profile across the arcjet exit plane is plotted in Fig. 12 for the 900 W case. There is a relatively small variation in temperature across the exit plane, ranging from 750 to 1120 K. The asymmetry that was apparent in the raw data is also evident here, with the peak temperature located at $z = -2$ mm, rather than along the centerline as expected. The asymmetry appears again in the density profile shown in Fig. 13, except that the peak density is located at $z = +2$ mm. The shape is more peaked than for temperature, with the maximum density slightly more than double the minimum.

The temperature profiles measured at the five power levels are plotted in Fig. 14. Similar asymmetries are evident to varying degrees in all cases. The maximum temperature always occurs at either $z = -2$ or $z = -4$ mm. The Temperatures generally rise across the entire exit plane as the power is increased. This behavior is illustrated in Fig. 15, where the maximum measured temperature is plotted as a function of arcjet power. The maximum temperature was chosen instead of the centerline temperature in order to allow a consistent quantity to be compared between profiles of varying shape. The results range from $T_{max} = 960$ K at 800 W to 1850 K at 1400 W, with a relatively smooth upward trend associated with increasing power.
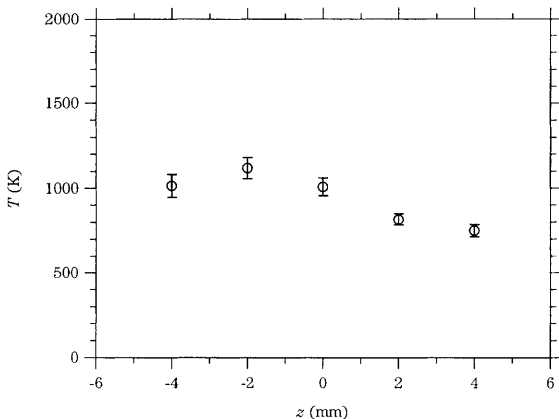

Fig. 14. Measured rotational temperature versus radial positions for five power levels
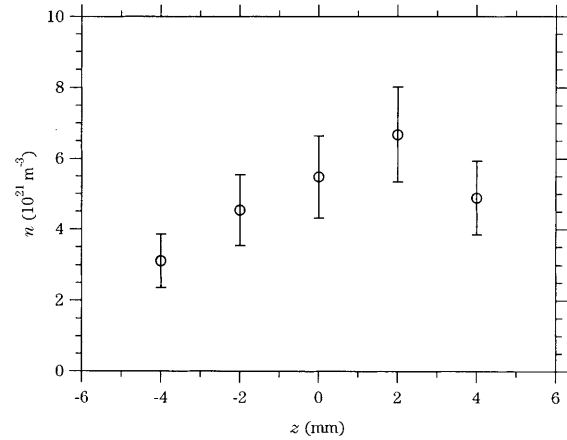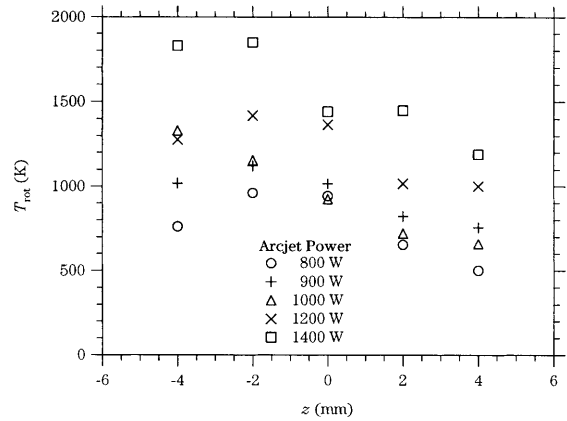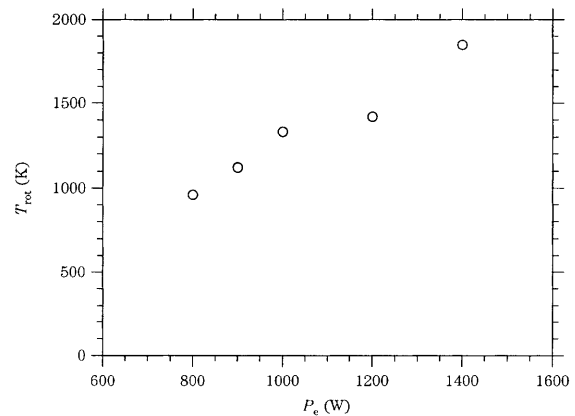

Fig. 15. Measured maximum rotational temperature versus arcjet power level

The corresponding density profiles are plotted in Fig. 16. Again, the profiles were all asymmetric, with the maximum density at $z = +2$ mm except for the 800-W power level. The densities range from 2.8×10^{21} to 8.8×10^{21} m^{-3}, all below the predicted value of 9×10^{21} m^{-3}. This difference is not surprising, since that prediction was based on the assumption that the exhaust was 100% H_2 at a uniform velocity.
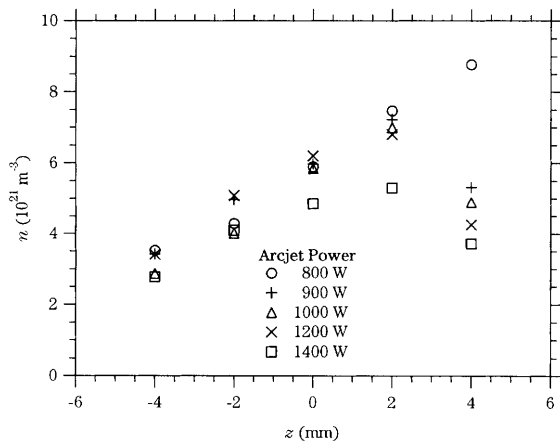

Fig. 12. Measured rotational temperature versus radial position for the 900-W power level

Fig. 16. Measured molecular hydrogen density versus radial positions for five power levels

4 Discussion

The H_2 rotational temperatures were compared to previous experimental results taken in our laboratory on the same arcjet Flow. The H translational temperature was previously measured on the same facility using LIF and emission of the Doppler-broadened Balmer α line. In the LIF study [5], the mass flow rate was reported as $13.7\,\mathrm{mg\,s^{-1}}$ (versus $13.3\,\mathrm{mg\,s^{-1}}$ here) and the power levels were 870, 1000, and 1500 W. This LIF data was re-analyzed to account for Stark broadening [20] and the resulting temperatures are significantly lower than the originally published data. The emission spectra were collected with a flow of $13.3\,\mathrm{mg\,s^{-1}}$ and $P = 1500\,\mathrm{W}$, and were Abel inverted to give spatially resolved data. Figure 17 shows a comparison of the exit-plane temperatures from Raman (1400 W), LIF (1500 W), and emission. The re-analyzed LIF results show the most peaked temperature distribution, reaching a maximum of 3400 K on axis, and in agreement with the more recent emission measurements of temperature. The Raman temperatures are the lowest of all, except near the edges, where all methods give similar values. However, the Raman temperatures are consistent with the absorption measurements of Pollard [12] which gave $T_{\mathrm{rot}} = 1500\,\mat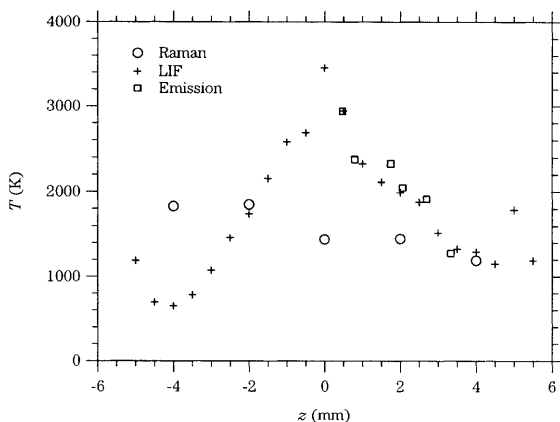hrm{K}$ averaged across the exit plane. It is noteworthy that while all of the distributions in the various temperatures measured are slightly asymmetric, the Raman measurements of *rotational* temperature seem to have the opposite asymmetry of in comparison to the distributions of translational temperatures shown. The assymetry is believed to be caused in part by a slight misalignment of the cathode with respect to the nozzle of the arcjet. It is seen that the measured rotational temperature is high where the molecular hydrogen density is low, and where the translational temperatures measured previously are also relatively low. At present, we have no explanation for the opposite asymmetries in the temperature fields, but suspect that it is due to an asymmetry in the overall flowfield within the nozzle.

These temperature measurements suggest the arc-ignited flow is not in rotational–translational equilibrium. This result is not entirely unexpected, since the cold-flow also showed significant rotational non-equilibrium. At the higher temperatures in the arc-ignited case, the rotational collisional number Z_{rot} decreases, which should bring the flow closer to equilibrium. However, the density is roughly an order of magnitude lower, which will have a counteracting effect by reducing the number of collisions. The lower rotational temperatures can potentially be explained by considering whether H_2 should be in rotational equilibrium as it diffuses to the center. The number of collisions an H_2 molecule would undergo while moving from the nozzle wall to the center is proportional to Kn^{-1}. The mean-free path was estimated for H_2 in H_2 (since the flow is predominantly H_2) using the tabulated value at room temperature and scaling as n^{-1}. At the throat $\lambda \approx 0, 6\,\mathrm{\mu m}$, so $Kn^{-1} \approx 500$. Since $Z_{\mathrm{rot}} \approx 60$ at 2000 K, then $Kn^{-1} \gg Z_{\mathrm{rot}}$ and the flow is likely near rotational equilibrium. However, at the exit plane $\lambda \approx 500\,\mathrm{\mu m}$ and $Kn^{-1} \approx 10$, so $Kn^{-1} \ll Z_{\mathrm{rot}}$. Hence near the exit plane the density is sufficiently reduced that H_2 molecules could be transported to the center without undergoing enough collisions to maintain rotational–translational equilibrium. Molecules colliding with the wall are expected to equilibrate at the wall temperature which has been estimated as $\approx 1700\,\mathrm{K}$ [1]. Hence the walls provide a source of H_2 with a rotational temperature comparable to that measured in the flow.

5 Summary

Raman scattering measurements of H_2 density and temperature were made at the exit plane of a 1-kW-class hydrogen arcjet thruster. Unlike in the cold-flow studies reported previously, pulsed-laser excitation was used in this study to improve the SNR in this high-background environment. Quantum-limited detection was achieved through the use of gated photon counting and a high-power Nd:YAG laser. Radial profiles of rotational temperature and density at the exit plane were measured for five power levels. In all cases the profiles were asymmetric about the arcjet centerline. The temperature profiles were compared with the translational temperatures of H from LIF studies and the bulk temperature from continuum simulations. The rotational temperatures were significantly lower than the other results, implying the flow is not in translational–rotational equilibrium. This finding is not so surprising, since results from the cold-flow studies and simple calculations indicate that rotational equilibrium is unlikely under cold-flow conditions. These results

Fig. 17. Comparison of temperature versus radial position from Raman scattering, LIF, and emission for $P \approx 1500\,\mathrm{W}$

also suggest that the predictive capabilities of numerical simulations of such flows would be enhanced by incorporating a rotational energy transfer mechanism. References

References

1. G.W. Butler, A.E. Kull, Q. King: AIAA Paper 94-2870, 30th AIAA/ASME/SQE/ASEE Joint Propulsion Conference, June 1994, Indianapolis, IN
2. S. Miller, M. Martinez-Sanchez: Paper IEPC 93-218, 23rd International Electric Propulsion Conference, September 1993, Seattle, WA
3. I.D. Boyd, D.R. Beattie, M.A. Cappelli: J. Fluid Mechan. **280**, 41 (1994)
4. I.D. Boyd: Phys. Fluids **9**, 3086 (1997)
5. J.G. Liebeskind, R.K. Hanson, M.A. Cappelli: Appl. Opt. **32**, 6117 (1993)
6. P.V. Storm, M.A. Cappelli: AIAA J. **34**, 853 (1996) ; P.V. Storm, M.A. Cappelli: Appl. Opt. **37**, 486 (1998)
7. D.H. Manzella, M.A. Cappelli: AIAA Paper 92-3564, 28th AIAA/SAE/ASME/ASEE Joint Propulsion Conference, July 1992, Nashville, TN
8. J. Pobst, I. Wysong, R. Spores: Paper AIAA-95-1973, 26th Plasmadynamics and Lasers Conference, June 1995, San Diego, CA
9. I.J. Wysong, J.A. Pobst: Appl. Phys. B **67**, 193 (1998)
10. P.V. Storm, M.A. Cappelli: J. Quant. Spectrosc. Rad. Transfer **56**, 919 (1996)
11. J.E. Pollard: AIAA Paper 92-2966, 23rd AIAA Plasma Dynamics and Lasers Conference, July 1992, Nashville, TN
12. J.E. Pollard: Paper IEPC 93-132, 23rd International Electric Propulsion Conference, September 1993, Seattle, WA
13. D.R. Beattie, M.A. Cappelli: AIAA Paper, 28th AIAA/SAE/ASME/ASEE Joint Propulsion Conference, July 1992, Nashville, TN
14. D.K. Veirs, G.M. Rosenblatt: Journal of Molecular Spectroscopy **121**, 401 (1987)
15. L. Wolniewicz: J. Chem. Phys. **78**, 6173 (1983)
16. L.A. Rahn, R.L. Farrow, G.J. Rosasco: Phys. Rev. A **43**, 6075 (1991)
17. A. Weber: In *The Raman Effect: Vol. 2*, ed. by A. Anderson (Marcel Dekker, New York 1973)
18. A.L. Ford, J.C. Browne: Atomic Data **5**, 305 (1973)
19. D.E. Jennings, L.A. Rahn, A. Owyoung: Astrophysical Journal **291**, L15 (1985)
20. D.R. Beattie: Ph.D. Thesis, Mechanical Engineering Department, Stanford University (1995)